



The Role of Thermodynamics on Northern Labrador Sea Ice Trends and Variability

M. N. Wang, B. Richaud & E. C. J. Oliver

To cite this article: M. N. Wang, B. Richaud & E. C. J. Oliver (06 May 2025): The Role of Thermodynamics on Northern Labrador Sea Ice Trends and Variability, Atmosphere-Ocean, DOI: [10.1080/07055900.2025.2497245](https://doi.org/10.1080/07055900.2025.2497245)

To link to this article: <https://doi.org/10.1080/07055900.2025.2497245>



© 2025 The Author(s). Published by Informa UK Limited, trading as Taylor & Francis Group



Published online: 06 May 2025.



Submit your article to this journal [↗](#)



View related articles [↗](#)



View Crossmark data [↗](#)

The Role of Thermodynamics on Northern Labrador Sea Ice Trends and Variability

M. N. Wang^{1,*}, B. Richaud², and E. C. J. Oliver¹

¹*Department of Oceanography, Dalhousie University, Halifax, NS, Canada*

²*Earth and Life Institute, Université catholique de Louvain, Louvain-la-Neuve, Belgium*

[Original manuscript received 12 August 2024; accepted 29 March 2025]

ABSTRACT Long-term changes and year-to-year variability in sea ice conditions on the northern Labrador (Nunatsiavut) coast and shelf have important influences on regional climate, marine ecosystems, and coastal communities. The drivers of sea ice variability in this region are poorly understood despite being critical for planning for future changes. Here, we evaluate the spatial and temporal trends and variability of sea ice area, concentration, thickness, and volume over the Labrador Shelf between 1979 and 2021 based on Canadian Ice Service sea ice charts. We characterise the seasonal cycle into two phases: a growth phase (December to January) and a peak phase (February to April). We then use Empirical Orthogonal Function analysis on mean ice thickness to identify the dominant modes of variability, and use correlations and simple physical models to investigate the relationships between these modes and thermodynamic forcing variables. Around 68% of the total variability can be explained by the first two modes (Mode 1: 52.6%; Mode 2: 15.2%). The first mode represents sea ice volume changes across the entire shelf, mainly driven by remote air temperature variations, with a smaller but non-negligible influence from local anomalies. The second mode represents a cross-shelf dipole structure that may be linked to the dynamic effects of winds and ocean currents.

RÉSUMÉ [Traduit par la rédaction] Les changements à long terme et la variabilité annuelle des conditions de la glace de mer sur la côte et le plateau du nord du Labrador (Nunatsiavut) exercent des influences importantes sur le climat régional, les écosystèmes marins et les collectivités côtières. Les facteurs de variabilité de la glace de mer dans cette région sont mal compris, bien qu'ils soient essentiels à la planification des changements futurs. Nous évaluons ici les tendances spatiales et temporelles et la variabilité de la superficie, de la concentration, de l'épaisseur et du volume de la glace de mer sur le plateau du Labrador entre 1979 et 2021, en se fondant sur des cartes des glaces de mer du Service canadien des glaces. Nous caractérisons le cycle saisonnier en deux phases : une phase de croissance (décembre à janvier) et une phase de pointe (février à avril). Nous utilisons ensuite l'analyse des fonctions orthogonales empiriques sur l'épaisseur moyenne de la glace pour identifier les modes dominants de variabilité, et nous utilisons des corrélations et des modèles physiques simples pour étudier les relations entre ces modes et les variables de forçage thermodynamiques. Environ 68% de la variabilité totale peut être expliquée par les deux premiers modes (mode 1 : 52,6%; mode 2 : 15,2%). Le premier mode représente les changements de volume de glace de mer sur l'ensemble du plateau, principalement induits par les variations de la température de l'air à distance, avec une influence plus faible, mais non négligeable des anomalies locales. Le second mode représente une structure dipolaire entre les plateaux qui peut être liée aux effets dynamiques des vents et des courants océaniques.

KEYWORDS Sea ice; variability; Canadian east coast; labrador; nunatsiavut

1 Introduction

Sea ice is a vital component of the Arctic and sub-Arctic oceanographic systems, serving as a key regulator of ocean-atmosphere exchanges. The northern Labrador Shelf (LS), located off Nunatsiavut, the northeast coast of Canada (Fig.

1), experiences seasonal ice cover which impacts the regional climate (Kvamstø et al., 2004), serves as a habitat for a diversity of marine species and sympagic fauna, and is integral for Labrador Inuit whose livelihoods are tightly linked to the ice (Brice-Bennett, 1977). Past sea ice conditions and

*Corresponding author's email: may.wang@dal.ca

© 2025 The Author(s). Published by Informa UK Limited, trading as Taylor & Francis Group. This is an Open Access article distributed under the terms of the Creative Commons Attribution-NonCommercial-NoDerivatives License (<http://creativecommons.org/licenses/by-nc-nd/4.0/>), which permits non-commercial re-use, distribution, and reproduction in any medium, provided the original work is properly cited, and is not altered, transformed, or built upon in any way. The terms on which this article has been published allow the posting of the Accepted Manuscript in a repository by the author(s) or with their consent.

their drivers for this region have not been well documented in the scientific literature, but are essential for understanding those in the present and future. This paper investigates the role of thermodynamic forcing on the long-term trends (1980–2021) and interannual variability of sea ice on the LS.

Understanding the sea ice response to atmospheric and oceanic forcing requires addressing the relative roles of thermodynamic and dynamic processes, which are not consistent across temporal and spatial scales. In the high Arctic, warming atmospheric temperatures are the dominant driver of sea ice decline (Meier & Stroeve, 2022). Studies on the Newfoundland and Labrador Shelf (e.g. Deser et al., 2002; Peterson et al., 2015; Prinsenberget al., 1997) have found that thermodynamics play a key role on regional sea ice variability. Sea ice metrics in the neighbouring Gulf of St. Lawrence have also been found to be driven by air temperature (Galbraith, Sévigny et al., 2024). Despite these findings, the drivers of interannual variability and trends specific to the LS remain unclear, as they are complexly linked to a combination

of local (LS-scale) growth and non-local advection. For instance, Cyr et al. (2022) found that winter air temperatures at Cartwright correlate strongly with ice metrics on the Newfoundland Shelf but not offshore of Cartwright, indicating that strong ice cover is associated with cold air temperatures in the source area even after it is advected away.

The sea ice composition on the LS is spatially complex, and different patterns of variability are found amongst regions. The ice originates from multiple sources, including local thermodynamic formation and advection from remote sources. Advection of sea ice onto the LS occurs along three major pathways: the Baffin Island Current (BIC), the West Greenland Current (WGC), and outflow from Hudson Bay (Fig. 1; Loder et al., 1998). The relative contributions of these sources vary seasonally and interannually, depending on both local and remote atmospheric and oceanic conditions (Cuny et al., 2005). The WGC, a northward extension of the East Greenland Current, transports a large fraction of Arctic exports from Fram Strait into Baffin Bay (Serreze & Francis, 2006). It flows along the eastern side of Davis Strait where it circulates cyclonically around Baffin Bay. Outflows from the Canadian Arctic Archipelago combined with the WGC form the southward flowing BIC, which transports sea ice along the western side of the Baffin Bay to the Labrador Sea (Tang et al., 2004). A smaller fraction of sea ice enters the LS through Hudson Strait (Straneo & Saucier, 2008). Nearly all of the pack ice on the LS is of advective origin (Symonds, 1986), and ice floes can originate anywhere along these pathways as far upstream as the Arctic Ocean. A large fraction of pack ice on the LS originates from the northern Labrador Sea, where sea ice production (mostly first-year ice) is modulated by the amount of available freshwater in the region (Close et al., 2018). On the LS, the Labrador Current, composed of two major branches, dominates the surface circulation. The main (offshore) branch of the Labrador Current is a strong current (mean speed 25 cm/s at the surface, Han et al., 2008) that flows along the continental slope (1000 m isobath) and forms the thermohaline front over the continental shelf that separates cold and fresher shelf waters from relatively warm and salty North Atlantic waters. The inshore branch near the coast is relatively weak, with surface velocities roughly half of those of the main branch (Lazier & Wright, 1993) and is primarily an extension of the outflow from Hudson Strait (Florindo-López et al., 2020).

Sea ice conditions on the LS, including the length and timing of the sea ice season, exhibit strong interannual variability (Cavaliere & Parkinson, 2012; Close et al., 2018; Deser et al., 2002; Peterson et al., 2015; Prinsenberget al., 1997). Freeze-up and break-up dates can vary annually by over a month (Canadian Coast Guard, 2022), and the relative contributions of advective sources vary seasonally and interannually, depending on both local and remote atmospheric and oceanic conditions (Cuny et al., 2005). Variability of local air and sea surface temperatures may affect the integrity of landfast ice, and anomalously warm temperatures can increase melt rates (or limit growth rates) of advected pack ice on the shelf. In addition, the LS is subject to frequent

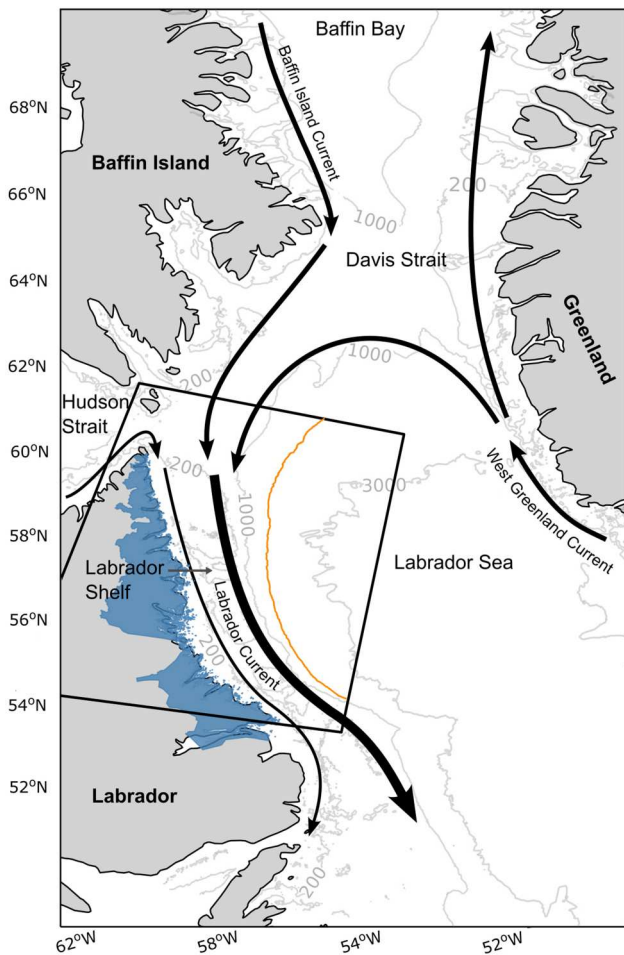


Fig. 1 Schematic of the general region and the study domain. The current systems are shown as black arrows. The 200 m, 1000 m and 3000 m bathymetric contours are shown in grey. The blue shaded region is Nunatsiavut and the black box represents the study domain. The orange line is the 15% contour of 1980–2021 March and April mean ice concentration from the CIS charts.

storms during the fall and winter months which can break up the ice and inhibit ice growth (Parkinson & Comiso, 2013). The presence of the Labrador Current System and strong persistent winds make the sea ice in this region highly dynamic. The goal of this study is to answer the question: how much of the total sea ice variability can be explained by thermodynamics? Quantifying this relationship is critical for improving ice and weather forecasts and making predictions about the sea ice response to future climate change.

In this paper, we examine the thermodynamic drivers on temporal and spatial variability of sea ice on the LS using 41 years of sea ice data from the Canadian Ice Service (CIS) with a specific focus on mean ice thickness (the product of ice concentration and thickness per grid cell). The data and methods are described in Sections 2 and 3. In Section 4, we show that the seasonal cycle of sea ice is dominated by the variability of sea ice thickness transported onto the shelf. The long-term trends are negative for sea ice area, thickness, and volume nearly across the entire domain. The two leading modes of sea ice variability derived from Empirical Orthogonal Function (EOF) analysis and their relation to atmospheric and oceanic variables during 1980–2021 are presented in Section 5. We show that the majority of sea ice variability is driven by remote air temperature variations. The discussion and conclusion are in Sections 6 and 7.

2 Data

a Sea ice

We use sea ice data from the CIS Digital Archive (CISDA: <https://iceweb1.cis.ec.gc.ca/Archive/>). The CISDA is a compilation of regional weekly ice charts derived from expert-analysed synthetic aperture radar imagery integrated with all available real-time information on sea ice including oceanographic and weather conditions and visual observations from ships and aircraft. These ice charts are provided as ArcInfo E00 format shapefiles. The CIS represents sea ice conditions using the World Meteorological Organization (WMO) egg code, assigning these to polygons each of relatively uniform sea ice conditions. Ice attributes including concentration and stage of development are contained in each egg as a separate data column and are the two variables used in this study. Sea ice concentration (*SIC*) represents the percent of ice cover within a defined area (in tenths) which we convert to percent. Stage of development, or stage of growth, is a qualitative metric used to categorise ice types based on age, and we use it here to estimate ice thickness (*SIT*; Table 1). The egg code convention divides each ice floe into a maximum of three ice types: thickest, second thickest, and third thickest. Each ice type has an associated stage of development (thickness) and partial concentration which combined sum up to the total concentration of the floe. In this study, we use the average ice thickness of each floe by multiplying the ice thickness of each ice type with their respective partial concentration.

Prior to 1983, the CIS used a different method of estimating stages of ice growth that involved a larger (less precise) range

TABLE 1. World Meteorological Organization (WMO) ice types (stage of development) and their conventional codes as depicted on the CIS chart products and associated thickness ranges.

Stage of development	Code	Probable thickness range (cm)	Thickness used (cm)
New ice	1	<10	5
Grey ice	4	10–15	12.5
Grey-white ice	5	15–30	22.5
First-year ice	6	≥30	95
Thin first-year ice	7	30–70	50
Medium first-year ice	1.	70–120	95
Thick first-year ice	4.	>120	160
Old ice	7.	–	250
Second-year ice	8.	–	250
Multi-year ice	9.	–	250

Note: Each code is converted to a single thickness value estimated from the midpoint of the associated thickness range. Thickness values for old ice, second-year ice, and multi-year ice were estimated from the literature.

for first-year ice (FYI). We follow the suggestion by Galbraith, Chassé et al. (2022) to avoid underestimation of FYI thickness by using an average FYI thickness of 95 cm instead of the 60 cm recommended by the CIS. Also, *SIT* ranges for old ice, second-year ice, and multi-year ice (MYI) are not provided as the thicknesses for these ice types range widely, and very limited data exist on for the LS. Barber et al. (2018) measured MYI floes around the east coast of Newfoundland (south of the LS) and reported thicknesses of 5 m. In the Arctic around Nares Strait, mean thicknesses have been reported between 2.5 m (Dunbar, 1973) to 5 m (Haas et al., 2010). We assign a conservative estimate of 2.5 m for each of these ice types on the LS. We also note that the CIS does not report stages of development for landfast ice, so we mask it out in our study by removing data at locations where the frequency of landfast ice presence is greater than 20%.

The CIS generates ice charts separately for a number of regions in Canada and coastal Labrador is partly included in both the Hudson Bay region (central and northern Labrador) and East Coast region (central and southern Labrador). Since our focus is on the northern coast (Nunatsiavut) we use the Hudson Bay charts. We rasterise Hudson Bay regional ice charts for the years 1979 to 2021 (inclusive) onto a 1 km × 1 km grid. This provides a gridded spatiotemporal (1 km spatial resolution, approx. weekly temporal resolution) data set of *SIC* and *SIT*. We analyse a subset of the Hudson Bay region, using the “common boundary” (area which is common to the whole period; Canadian Ice Service, 2007) so that we only consider the northern Labrador coast (Nunatsiavut) and shelf (Fig. 1, black box).

The CIS ice charts only note ice melt using symbols for stage of melting (see Table 3.5 in Canadian Ice Service, 2005). Stage of development can be interpreted as stage of ice growth and it remains at the winter max during the melt season. In our dataset this manifests as ice keeping its maximum thickness until it disappears (i.e. *SIC* reduces to 0) at which point the *SIT* value switches to 0. For this

reason, we remove the melt phase and all ice-free months (defined as May 1 to November 30) from the dataset. Our analyses on sea ice trends and variability thus only focusses on the growth phase (December 1 to January 31) and peak phase (February 1 to April 30) of the sea ice season. We reference each ice season by the year of the peak months (e.g. the 2010 season is December 1, 2009 to April 30, 2010). We refer to ice thickness (*SIT*) as the thickness of ice present (m) and mean ice thickness (*H*) as the average thickness of ice over an area including contribution of open water (m). *H* is calculated as the product of ice thickness and concentration ($H = SIT \times SIC$). Both variables are important in sea ice physics: *SIT* governs thermodynamic processes (i.e. growth and melt), while *H* is key in mass conservation equations. We define sea ice area (*SIA*) as the total area of ice cover in the domain (not including open water) and sea ice volume (*SIV*) as the domain integrated product of *SIA* and *SIT*.

b Atmosphere and ocean state variables

We obtain hourly fields of atmospheric state variables at $1/4^\circ$ resolution from 1979 to 2021 (2 m surface air temperature (SAT), eastward and northward components of 10 m winds, incoming surface longwave (thermal) radiation, incoming surface shortwave (solar) radiation and mean surface latent heat flux) from The European Centre for Medium-Range Weather Forecasts Reanalysis v5 (ERA5; Hersbach et al., 2023). We also extract daily mean SAT data from 1980–2020 at Nain, NL (56.551°N , 61.682°W) from the Adjusted and Homogenized Canadian Climate Data (AHCCD) website (NAIN; ECCC, 2018). We obtain hourly fields of ocean state variables at $1/12^\circ$ from 1993 to 2021 (sea surface temperature (SST) and eastward and northward components of surface currents) from The Copernicus Global $1/12^\circ$ Oceanic and Sea Ice GLORYS12 Reanalysis (GLORYS; Jean-Michel et al., 2021). We subset the ERA5 and GLORYS data to 45°N to 59°N (latitude) and 60.5°W to 45°W (longitude). Annual North Atlantic Oscillation (NAO) indices are retrieved from Hurrell (2003) for the period 1980–2021. Monthly Arctic Oscillation (AO) and El-Niño Southern Oscillation (ENSO) indices are retrieved from the National Oceanic and Atmospheric Administration’s (NOAA) Climate Prediction Center (AO: https://www.cpc.ncep.noaa.gov/products/precip/CWlink/daily_ao_index/ao_index.html, ENSO: <https://www.cpc.ncep.noaa.gov/data/indices/soi>) and averaged annually over the period 1980–2021.

3 Methods

a Seasonal means, anomalies, and trends

We calculate seasonal means and anomalies and long-term trends from the weekly sea ice variables and hourly mean atmosphere and ocean state variables over the period 1980–2021 and separate each season into growth (December to January) and peak (February to April) phases. Since the frequency of the ice charts is not regular over time, we calculate

weighted seasonal and phase means such that each month is weighted equally. We then subtract this climatology from the original data to obtain anomalies to represent deviations from a normal ice season. We calculate daily means and anomalies following the same treatment for the atmospheric and ocean state variables. We calculate linear trends using linear regression, and associated p-values which we show with each trend to indicate statistical significance. When reporting trends, a significant trend is one where $p < 0.05$.

b Statistical methods

We use Empirical Orthogonal Function (EOF) analysis to identify the dominant spatiotemporal modes of variability of *H* on the LS during the period 1980–2021. EOF analysis essentially decomposes the dataset into a set of linearly independent modes, which are patterns of spatial variability multiplied by time-varying principal components. Each mode is chosen to maximise variance; this method is most useful when a majority of the total variance in the original dataset is represented by relatively few modes (e.g. Davis, 1976, Appendix B). We seasonally average monthly anomalies of *H* and then detrend over the 41-year period, giving an annual timeseries for our EOF input. The output of the EOF is a set of n modes, where n is the number of rows (in our case these are seasons, so we get 41 modes), which are ordered by the fraction of total variance accounted for by each mode. Each mode comes with a spatial pattern (EOF pattern) which represents the spatial structure of that mode and a time series (principal component, PC) which represents how that structure varies in time. For display purposes, we normalise the PC time series to unit variance and re-scale the EOF patterns by the standard deviation of their respective PC time series. This allows us to interpret the EOF patterns roughly in the units of the source data (e.g. m for *H*). To determine which modes of the EOF analysis are statistically significant, we use the “Rule N” method by Overland and Preisendorfer (1982).

We also examine the relationships between the dominant modes of variability and potential regional forcing. We correlate (Pearson correlation) the PC time series for each mode with time series of detrended atmospheric and SST anomalies at each location. We then map this correlation for each combination of mode and forcing variable over our study region.

c Thermodynamic ice growth models

To investigate the role of local thermodynamic forcing on sea ice variability we implement two thermodynamic ice growth models. These models provide a good first-order approximation of sea ice variability due to thermodynamic effects alone (i.e. ignoring dynamical and mechanical effects on ice growth due to convergence or the formation of ridges and keels).

The first model is an empirical model based on freezing degree days (FDD) which assumes that ice growth is only a function of air temperature (T_a). For days where T_a is less

than the freezing temperature T_f , $SIT = 1.33\theta^{0.58}$ (Lebedev, 1938), where $\theta = \int_0^t (T_f - T_a) dt$ is the cumulative freezing degree days (in °C days). There are two problems with this model: (1) ice thickness in categories above FYI in the CISDA are based on an FDD model itself, and (2) it does not account for the complete physics (i.e. the full thermodynamic balance). To address these problems, we introduce a second model, referred to here as the heat flux model (HFM), which is a physical model based on a heat flux balance. In this model, SIT is estimated using a 1-layer heat flux balance adapted from Semtner (1976). We calculate the rate of ice growth, $\frac{\partial SIT}{\partial t}$, from the following conditional expression:

$$\frac{\partial SIT}{\partial t} = \begin{cases} -\frac{1}{L_i} (k_i \frac{T_s - T_b}{H} + F_w) & T_s < T_m \\ -\frac{1}{L_i} ((1 - \alpha)F_{inSW} + F_{netLW} + F_{sens} + F_{lh} + F_w) & T_s = T_m \end{cases} \quad (1)$$

where L_i is the latent heat of fusion for sea ice ($300 \times 10^6 \text{ J m}^{-3}$; Semtner, 1976), T_s and T_b are the ice temperatures at the ice surface and bottom (K), T_m is the sea ice melting point (0°C), α is the temperature-dependent ice surface albedo (0.8 for bare ice, 0.5 for melting ice; Goosse et al., 2000), k_i is the sea ice heat conductivity ($2.03 \text{ W m}^{-1} \text{ K}^{-1}$; Semtner, 1976). The heat flux terms (F) are positive into the ice and have units W m^{-2} . At the ice surface, F_{inSW} is the downward shortwave radiation, F_{netLW} is the net longwave radiation, F_{sens} is the sensible heat flux, F_{lh} is the turbulent latent heat flux and at the bottom F_w is the ocean heat flux. Incoming longwave (F_{inLW}), incoming shortwave (F_{inSW}), and F_{lh} are directly taken from ERA5 and F_{sens} is calculated from 10 m wind speeds and SAT (see Appendix A). F_{netLW} is calculated from $F_{inLW} - F_{outLW}$ where we assume the sea ice to behave as a perfect black body such that $F_{outLW} = \sigma T_s^4$ with σ the Stefan-Boltzmann constant, and $F_{netSW} = (1 - \alpha)F_{inSW}$. We fix T_b to the freezing point of seawater (-1.8°C). By doing so we have ignored the effects of the atmosphere cooling the ocean to its freezing point before the ice season, which would require a more complex model to resolve. The forcings are spatially averaged such that the inputs and outputs are one-dimensional time series. We ignore the snow layer and so the ice surface always corresponds to the ice-atmosphere interface. We solve the model using the standard Euler-backward scheme in the programming language of Python. For a complete model description and details on the setup, see Appendix A. Finally, we convert the solutions of the FDD model and the HFM to seasonal anomalies to match the sea ice (PC) time series.

Our model forcing data, ERA5, is from a model that assimilates sea ice data. To address this issue, we run the FDD model using NAIN SAT, which is an independent

data source, then compare these results to the FDD model using ERA5 SAT. We will show in Section 2 that the two data sources yield statistically indistinguishable results, and thus the forcing data used in our models are not driven by the presence or absence of sea ice.

The HFM takes in the ocean temperature (T_w) and the ocean heat flux (F_w) as free parameters. There are no direct measurements of F_w on the LS, but Wettlaufer (1991) observed values between $0\text{--}37 \text{ W m}^{-2}$ in Fram Strait and Yao et al. (2000) estimated values around 30 W m^{-2} during ice melt on the LS. 4 W m^{-2} is typically used for the central Arctic (Wagner & Eisenman, 2015). Since our season does not include the warm melting months, we model ice growth with upper limit of 20 W m^{-2} and a lower limit of 0 W m^{-2} .

The occurrence of ice on the Labrador Shelf arises from a combination of local growth and non-local advection into the domain. Advected ice can also grow thermodynamically immediately upstream (i.e. northern Labrador Sea) and/or could be advected in from still further upstream (e.g. Baffin Bay, Arctic Ocean). To evaluate local versus remote thermodynamic forcing, we use ice growth models under two scenarios. In Case 1, ice grows from an initial zero thickness throughout the season, with forcing applied over a larger domain that extends north to Davis Strait (domain displayed in Fig. 7). In this case we model ice growth that occurs upstream and along the path to the Labrador Shelf (LS). In Case 2, ice is initialised with a prescribed initial thickness (H_0) and is forced only with local conditions on the LS (domain displayed in Fig. 2). H_0 is assumed to be the thickness of ice that is advected into the domain and is based on monthly climatology (2016–2020) of ice thickness exports across Davis Strait (Howell et al., 2024). This isolates local thermodynamic effects to estimate ice growth while on the LS only. Mean ice drift speeds on the LS range from $10\text{--}50 \text{ cm/s}$ (Peterson & Symonds, 1988), giving transit times between 19 and 97 days (median 39 days) along its 837 km length. For Case 2, we run the model from December 1 to April 30 with a 1-day timestep for transit times of 19, 39, and 97 days. Ice growth on the LS, ΔSIT , is calculated as the model thickness at the end of the integration time minus H_0 , providing growth estimates as a function of transit time.

4 Seasonal climatology and long-term trends

The sea ice season on the LS typically starts in early December and ends in late June. It begins with landfast ice consolidating relatively quickly along the coast and new ice beginning to appear over the shelf (Fig. 33 in Canadian Coast Guard, 2022 and Fig. 7 in Cyr et al., 2024b). For the rest of the winter, pack ice covers the shelf and is made up of predominately FYI, with a small fraction of old ice floes and icebergs embedded within the main pack. An equilibrium ice edge forms each year and coincides with the thermohaline front along the edge of the shelf, and the frequency of ice presence drops east of this edge (Fig. 2a,b; it should be noted that the gradient in this transition zone is a consequence of

averaging the gridded data, but in the individual, weekly CIS ice charts the transition is actually quite sharp). When ice is present, it is typically thinnest along the shelf edge (Fig. 2f) and thickest over the northern half of the shelf. During the peak phase, the shelf is nearly 100% ice-covered (Fig. 2b), with notable exceptions being a polynya off the far north coast ($\sim 60^\circ\text{N}$) and some evidence of flaw leads along the edge of the landfast ice.

The domain averaged variables exhibit distinct seasonal patterns, with *SIA* peaking in February and remaining constant, while *SIT* and *SIV* continue to increase throughout the ice season (Fig. 3). The climatology of seasonal *SIV* is consistent with what Cyr et al. (2024b) reported (see Fig. 10 of their report). The spreads, measured between the 20th and 80th percentiles, indicate that the variances of the variables are out of phase (Fig. 3, shading). While the spread is largest in the growth phase for area, it peaks in the peak phase for *SIT* and *SIV*. The spreads also reach their maximum at different times: in January for *SIA* ($97 \times 10^3 \text{ km}^2$), in February for *SIT* (0.35 m) and in April for *SIV* (105 km^3).

Time series of phase-averaged *SIT*, *SIA*, and *SIV* anomalies display significant year-to-year variability as well as a notable downward trend (Fig. 4 and Table 2). Seasonal maximums of *SIV* and *SIA* have been reported in Cyr et al. (2024a, Fig. 11) to be $60\text{--}250 \text{ km}^3$ and $70 \times 10^3 \text{--} 200 \times 10^3 \text{ km}^2$ on the northern Labrador Shelf over the same time period. Normalized trends (trends normalised by their standard deviation) indicate that the variables are decreasing at a similar rate over time, with *SIT* and *SIA* decreasing faster than *SIV* (Table 2). Detrended anomalies (not shown) show clear signals of decadal variability, with notable *SIV* minimums in 1989 and 2011 in the growth phase and 1982, 1997 and 2021 in the peak phase. Cyr et al. (2024b) reported seasonal average *SIV* minimums on the northern Labrador Shelf in 2011 and 2021. The variability is larger in the peak phase for *SIV* (standard deviation: 63 km^3), *SIT* (0.19 m), and *SIA* ($47 \times 10^3 \text{ km}^2$) compared to the growth phase (13 km^3 , 0.10 m, $44 \times 10^3 \text{ km}^2$).

The linear trends for all variables calculated per pixel indicate that the amount of sea ice is not obviously decreasing everywhere on the LS (Fig. 5). Negative trends appear over almost the whole domain except for a strip adjacent to the landfast ice zone, but the trends on the shelf are relatively small and mostly not statistically significant. The strongest and only statistically significant trends in *H* (approx. -1 cm/year ; Fig. 5d)

appear along and to the east of the shelf edge during the peak phase. This region is not typically associated with heavy ice conditions, but these trends may indicate that there is a reduction of *SIV* at this location. *SIT* is decreasing over most of the shelf, especially in the peak phase (approx. -1 cm/year ; Fig. 5f), suggesting that ice that enters the LS is thinning. Stronger and statistically significant negative trends along the MIZ zone for *SIC* (approx. $-1\%/year$; Fig. 5a,b) indicate a reduction of ice cover eastward from the shelf edge.

5 Physical drivers of sea ice trends and variability

a Dominant modes of variability

We decompose detrended *H* anomalies into a set of statistically orthogonal modes of variability using an EOF analysis. Based on the ‘‘Rule N’’ test (Overland & Preisendorfer, 1982), the first four modes are statistically significant. We focus on Modes 1 and 2, which together explain 67.8% of the total variance in the dataset, while Modes ≥ 3 account for $< 7.3\%$ each. The most apparent difference between the first two modes is the monopole structure of Mode 1 versus the dipole structure of Mode 2 (Fig. 6a,c). Mode 1 (52.6%) corresponds to a monopole of anomalies of the same sign over nearly the entire domain which suggests that the associated forcing anomalies would be large in scale relative to the spatial scale of the LS. The entire northern end of the domain is dominated by relatively large anomalies with decreasing magnitudes towards the east and south. The largest anomalies are centred at the middle of the domain (Fig. 6a), resembling the climatology (Fig. 2b). Here, a PC mode value of ± 1 (e.g. $2021 = -1.04$) corresponds to roughly $\pm 0.16 \text{ m}$ and decreases to $\pm 0.05 \text{ m}$ at the southern end (Fig. 6b).

Mode 2 (15.2%) is a spatially asymmetric mode with different signs between nearshore/shelf and offshore regions (Fig. 6c). The poles are located in the northeast (NE) and southwest (SW) corners of the domain with the zero axis centred along the shelf edge. The maximum magnitude of this mode is less than that of Mode 1, which is roughly $\pm 0.11 \text{ m}$ at the SW pole axis for a PC mode value of ± 1 (e.g. $2013 = 1.0$). Over the rest of the shelf and the offshore region, the magnitudes are around $\pm 0.05 \text{ m}$.

The PC time series of Modes 1 (PC-1) and 2 (PC-2) both exhibit strong interannual variability and some decadal and multi-decadal variability. For example, PC-1 switches from a negative phase between 1998 and 2007 to a positive phase between 2007 and 2017, and PC-2 is in a negative phase between 1984 to 1997 and then a positive phase between 1997 and 2015 (Fig. 6b,d, red line). In many years, the signs of the sea ice anomalies on the shelf are opposite between the two modes (e.g. between 1998 and 2007, PC-1 anomalies are dominantly negative whereas PC-2 anomalies are dominantly positive). Power spectra for PC-1 and PC-2 (not shown) show that both modes have frequency peaks concentrated in the interannual band (between 0–5 years), with more variance in Mode 2. However, there are no statistically

TABLE 2. Trends of domain-averaged sea ice volume (*SIV*), thickness (*SIT*), and area (*SIA*) over the full-time period (1980–2021) from observations and derived from the heat flux model (HFM).

Phase	Volume (km^3/year)	Thickness ($10^{-2} \text{ m}/\text{year}$)	Area ($10^3 \text{ km}^2/\text{year}$)
Growth	-0.2 (-0.017)	-0.36 (-0.037)	-1.60 (-0.037)
Peak	-1.2 (-0.019)	-0.68 (-0.036)	-1.46 (-0.031)
Season	-0.4 (-0.013)	-0.29 (-0.021)	-1.12 (-0.27)
HFM	-1.2 (-0.025)	-0.23 (-0.036)	

Note: Normalized trends are reported in brackets. All trends are statistically significant ($p < 0.05$)

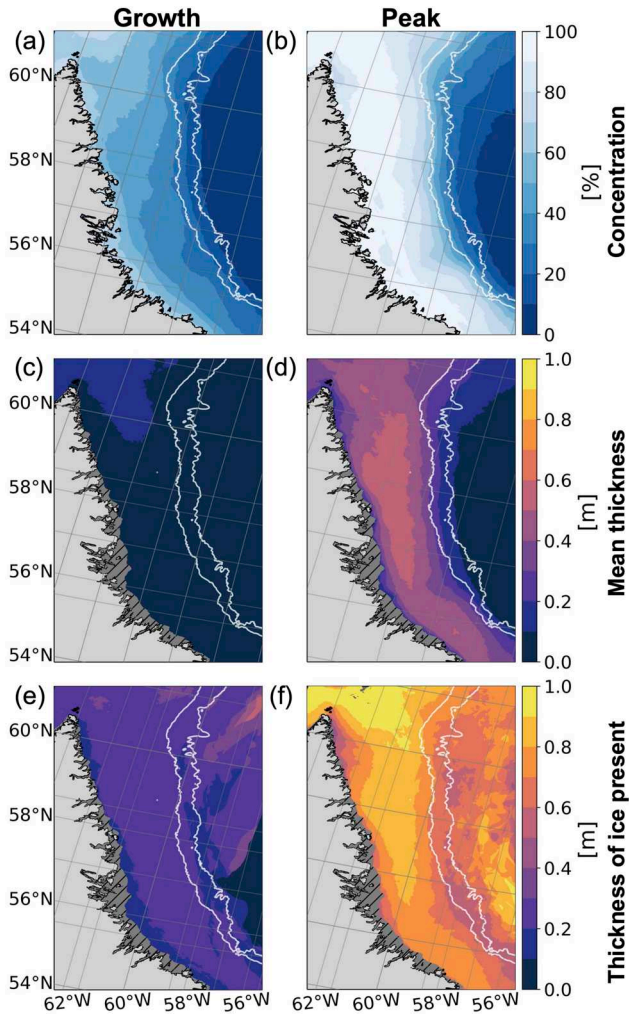


Fig. 2 Seasonal climatology of sea ice along the northern Labrador coast and shelf. Shown are climatological sea ice (a,b) concentration (SIC), (c,d) mean thickness (H) and (e,f) thickness of ice present (SIT) for (a, c, e) the ice growth phase (December and January) and (b, d, f) the peak ice phase (February to April). White lines depict the 1000 and 2000 m isobaths. The grey hatched area represents the landfast ice zone which is masked out for SIT and H in this study.

significant peaks (at the 5% confidence level, calculated based on Mitchell et al., 1966) in either mode. Therefore, we cannot determine a clear or dominant frequency component in either of the PC time series; although, it is clear that both time series exhibit variations on interannual to decadal time scales. Lagged autocorrelations (not shown) for both modes are weak ($|r| < 0.3$) and not statistically significant at the 5% confidence level at all non-zero lags, so we do not have evidence of any persistence in either time series.

b Role of thermodynamic forcing

1 SPATIAL CORRELATIONS WITH AIR TEMPERATURE ANOMALIES

To determine the potential physical drivers associated with each mode, we correlate PC-1 and PC-2 with possible forcing variables (SAT, SST, wind stress and surface

currents) for each pixel in the whole domain. Only the correlations with SAT exhibit sizeable area with statistical significance at the 5% confidence level. We compute lagged correlations ($-2, -1, 0, 1, 2$ months) between ERA5 SAT and PC time series. A lag of -1 correlates seasonally averaged temperature anomalies from November to March with the ice data from December to April. Negative lags consistently show stronger correlations than positive lags for both modes, suggesting that SAT has a lagged influence on sea ice. Note that the differences in correlations for each lag are small ($\leq O(10^{-1})$). The following results are for lag -1 .

Strong negative correlations between SAT and Mode 1 at lag -1 are evident across the entire domain (Fig. 7a). This indicates that rising air temperatures correspond to a reduction in H . The boundaries of these correlation maps are larger than the sea ice domain to capture correlations with SAT anomalies further north (upstream). In contrast, for Mode 2, the correlations are generally positive and weaker, except east of the shelf edge (Fig. 7b). Correlations with both modes are statistically significant at the 5% confidence level at all grid cells.

2 LOCAL VERSUS REMOTE FORCING

We further investigate thermodynamic-driven variability using a set of ice growth models. Despite the statistically significant correlations between SAT and PC-2, the dipole pattern of Mode 2 suggests that sea ice anomalies forced by domain-averaged SAT would result in patterns of a single sign (monopole) and thus be unrelatable to Mode 2. We therefore only test our models against Mode 1. Studying the relationship between ERA5 variables and sea ice may be biased since sea ice is assimilated into the ERA5 model (this is also the case for the correlation maps, Fig. 7). To test whether ERA5 variables are strongly constrained by the presence/absence of ice, we apply the FDD model using NAIN SAT (an independent data source which does not involve the assimilation of sea ice data). All ice growth models are applied in two cases (details in Section c). We then multiply modelled SIT with SIC to calculate seasonally averaged H anomalies (December 1 to April 30; Fig. 8a,b). In both cases, the FDD models using ERA5 and NAIN SAT produce statistically indistinguishable results for H anomalies ($r = 0.96, p < 0.05$), so the presence/absence of ice does not affect the ERA5 variables and either data source can be used for these models.

We present a total of four model outputs (Fig. 8, colored lines): FDD with NAIN SAT, FDD with ERA5 SAT, HFM with ERA5 forcing and $F_w = 0 \text{ Wm}^{-2}$ and HFM with ERA5 forcing and $F_w = 20 \text{ Wm}^{-2}$. PC-1 is strongly correlated with H from each model output when averaged across transit times ($0.60 < r < 0.71$). The composite mean thickness (average across models and transit times) correlates with PC-1 at 0.69 in Case 1 and 0.70 in Case 2, while correlations with total observations are slightly higher at 0.75 and 0.76. These results indicate that thermodynamic effects

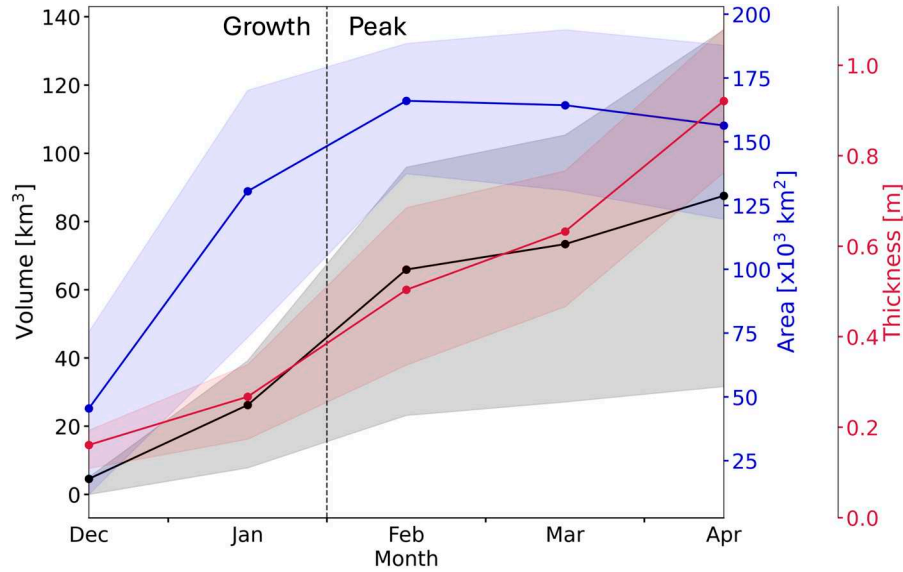


Fig. 3 Seasonal cycle of sea ice volume (*SIV*; black), thickness (*SIT*; red), and area (*SIA*; blue) for the period 1980–2021. The annual mean is represented by a solid line with shading between the 20th and 80th percentiles. The vertical dashed line separates the growth phase and the peak phase.

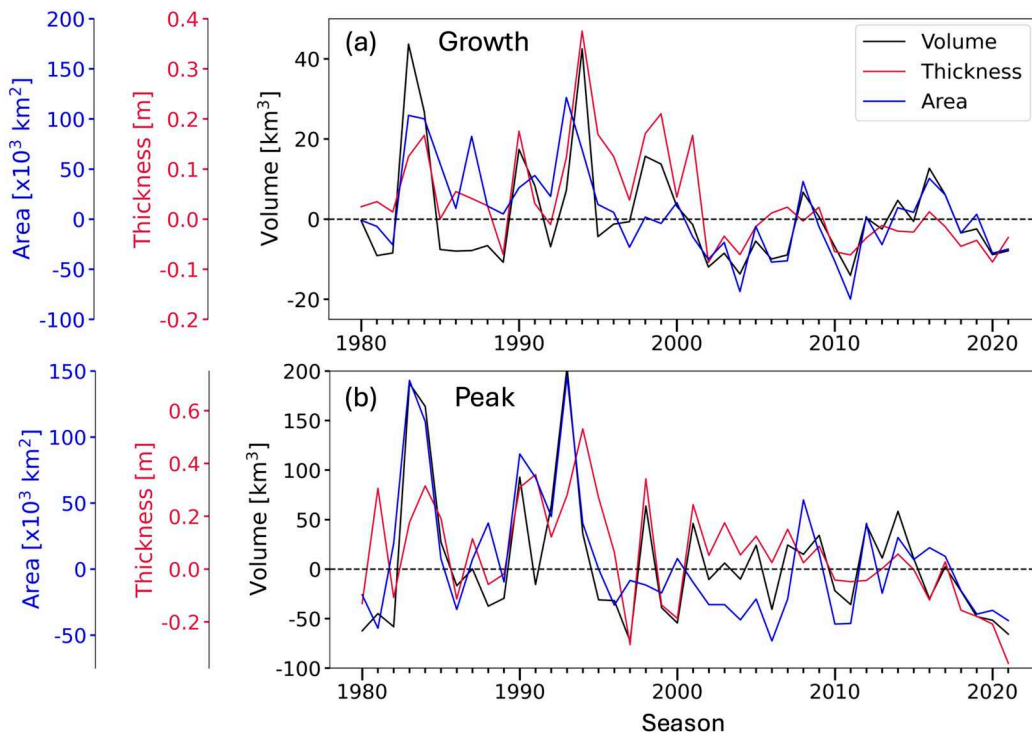


Fig. 4 Phase averaged anomalies of sea ice volume (*SIV*), thickness (*SIT*), and area (*SIA*). (a) Growth phase. (b) Peak phase. The variables are spatially averaged over the study domain with phase means removed to represent anomalies over the period 1980–2021.

(growth and melt) explain a substantial fraction of the total variance in the first EOF mode, with average r^2 values showing that $\sim 50\%$ of the variance is accounted for in both cases.

Since the local and remote thermodynamic anomalies are physically coupled, the similarity in r -values is not surprising. However, to assess the relative contributions of remote versus

local effects, we calculate the ratios of local ice growth (ΔSIT) to initial ice thickness (H_0) at each month, and average these ratios across each season. The results show that ice can grow 20–100% thicker than its initial thickness during transit, with a mean growth of $\sim 50\%$ (Fig. 8c). We note that we did not factor in transit times along the ~ 600 km distance from where H_0 is measured to the northern

edge of the LS. If we assume ice drifts at a relatively constant speed from Davis Strait to the LS, then about 2/3 of the ice growth we modelled in Case 2 would have occurred over this stretch, meaning that the average ice floe reaches most of its maximum thickness before it arrives on the LS. Overall, our findings highlight the significant role of thermodynamic forcing but reveal that the majority of sea ice variability is driven by thermodynamic anomalies upstream (i.e. in the source region), while local (i.e. LS-scale) forcing plays a non-negligible, but smaller role in the growth and peak stages of the ice season. We also correlate annual NAO, AO, and ENSO indices with PC-1 and PC-2 (not shown). However, no correlations were significant at the 5% confidence level ($p > 0.05$ in all cases).

Through a set of five model experiments, we examine the relative roles of each flux term from the heat flux model on *SIT* in Case 1. In each experiment a specific heat flux term is removed from the model forcing. Consider the total heat flux to be $F_T = \sum_i F_i$, where F_i represents the various flux terms (e.g. sensible heat flux, latent heat flux...see Eq. (1)). The solution with all forcing included is $H(F_T)$ (Fig. 9a). In our experiments where we remove a specific heat flux term F_i the solution is denoted $H(F_T - F_i)$. The difference between these solutions and the complete solution, $\Delta SIT = H(F_T) - H(F_T - F_i)$, represents the effect of each heat flux term on *SIT* (Fig. 9b). The standard deviation of these difference time series (Fig. 9c) indicate that the model is most sensitive to the effects of sensible heat (F_{sens}) and net longwave radiation (F_{netLW}). Shortwave radiation (F_{SW}) plays a secondary role. Ice-water heat flux (F_w ; here set to 4 Wm^{-2}) is weakly important and latent heat flux (F_{lh}) is negligible. Since F_{sens} and F_{netLW} are both physically linked with SAT (sensible heat through turbulent exchange across the ice surface and longwave radiation through the Stefan-Boltzmann law), this result suggests that the heat flux model largely represents the thermodynamic growth and melt effects of SAT anomalies between the source region and the LS.

The observed seasonal trends of *SIV* and *SIT* are noticeably similar to the trends calculated from the heat flux model (Table 2). Notably, the heat flux model appears to best represent the trend in *SIV* in the peak phase and *SIT* in the growth phase. This result suggests that a large part of the observed trend is attributed to thermodynamic forcing, and the heat flux model can reconstruct not only the total variability but also the long-term trend of observed *SIV* and *SIT*.

c Physical drivers of mode 2

The drivers of Mode 2 (12.9%) remain puzzling, as we did not find any significant correlation with individual external forcing variables. The positive correlation between SAT and Mode 2 is not thermodynamically plausible (or does not represent a physical mode), so we investigate a possible dynamical mechanism. We investigate the coupled effects of advection by currents and wind drift. We seasonally average ERA5 winds and GLORYS currents, excluding the melt and

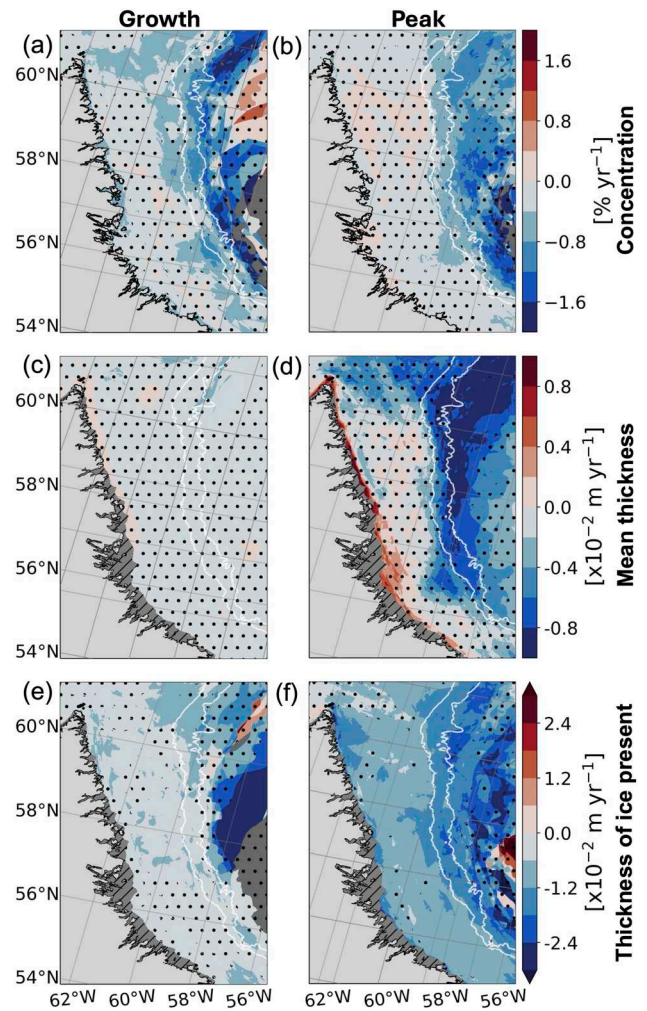


Fig. 5 Sea ice trends by variable and seasonal phase. Linear trends are shown for sea ice (a,b) concentration (*SIC*), (c,d) mean thickness (*H*) and (e,f) thickness of ice present (*SIT*) for the (a,c,e) growth phase and the (b,d,f) peak phase. Dots represent trends not significant at the 5% significant level. The grey hatched area represents the landfast ice zone which is masked out for *SIT* and *H* in this study.

ice-free months to match the CIS timeseries (December 1 to April 30). Winds are spatially averaged over the Labrador Shelf (Fig. 1, black box) and westerly wind strength is derived from the u-component of wind velocity, with strong westerlies defined as values above the climatological mean and weak westerlies defined as values below the mean. LC speed is calculated using the v-component of current velocities along a cross-shelf transect at 59°N (61.6°W to 59.2°W). Strong and weak LC speeds are similarly defined as speeds above and below the climatological mean. We then identify time periods for all combinations of weak or strong LC and westerlies. *SIC* anomalies are averaged over each time period to reconstruct spatial anomaly maps for each scenario (Fig. 10). Regardless of LC strength, westerlies appear to be associated with *SIC* anomalies: strong westerlies drive positive *SIC* anomalies on the LS, while weak westerlies drive negative *SIC* anomalies. However, the effect of the

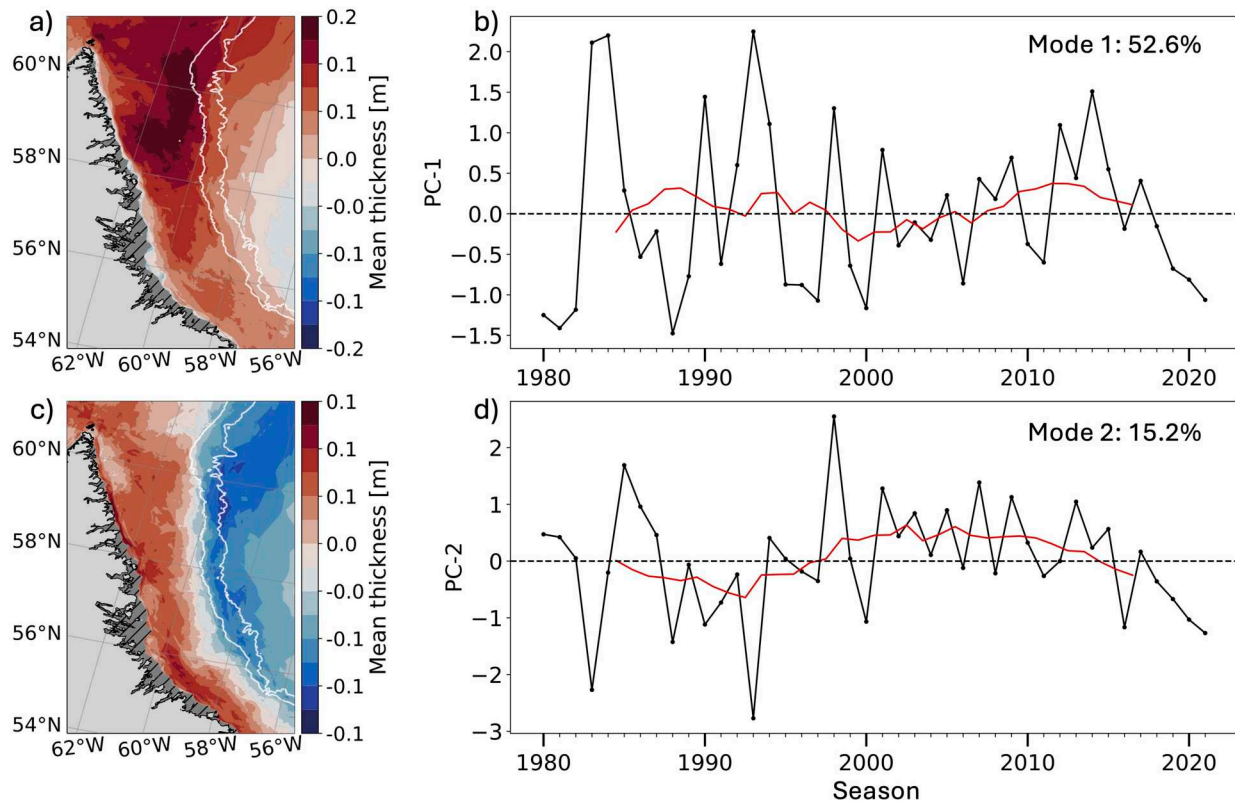


Fig. 6 Dominant modes of variability of mean ice thickness (H). Modes are shown as Empirical Orthogonal Function (EOF) patterns (left) and associated principal component (PC) time series (right; black line) of H for Mode 1 (top) and Mode 2 (bottom). 10-year running means of the PC time series are plotted with a red line. Each mode's percent variance explained is displayed in the upper right corner of the PC time series. The white lines on the maps represent the 1000 m and 2000 m isobaths. The grey hatched area represents the landfast ice zone which is masked out for ice thickness (SIT) and H in this study.

westerlies is more pronounced during a strong LC (Fig. 10a,b) than during a weak LC (Fig. 10c,d). This result suggests that there may be some coupled effect between ocean current and wind strength linked to the competing effect between westerly winds and the LC. Additionally, it may be possible to link local wind patterns influencing SIC anomalies to regional climate patterns such as the Icelandic Low and Labrador Sea-Baffin Bay ocean circulation. A more comprehensive dynamical model is needed to further investigate these potential ocean-atmosphere interactions linked to Mode 2.

6 Discussion

a Strengths and limitations of the thermodynamic ice growth models

Research efforts are becoming more and more reliant on state-of-the-art climate models (e.g. Global Climate Models) to study sea ice trends and variability. However, there is still no reliable sea ice forecasting product for the Labrador Shelf region. It has been shown that ice model skills to simulate the mean state is not correlated to model complexity (Massonnet et al., 2018), and simple models like the heat flux model presented here are an effective tool to isolate different physical processes governing sea ice conditions. In our study we have shown that the majority of the total sea

ice variability can be reconstructed if a few thermodynamic terms are known, even without considering mechanical (dynamic) mechanisms.

As with all models, the performance of the heat flux model is limited by the lack of in-situ data to validate the models, perhaps most importantly snow cover (Turnbull & Taylor, 2018). Consequently we must apply it under assumptions that do not accurately represent conditions on the LS. Ignoring the effects of snow and assuming seasonally constant ocean-ice heat flux are relatively large assumptions that could considerably affect how ice thickness variations are estimated. Also, since the CIS charts are not a sea ice thickness product, the thickness values are not entirely reliable. We show from a separate EOF analysis on SIC (not shown) that the EOF patterns look very similar to that of H . Thus, SIT and SIC are not thermodynamically independent, and so both thermodynamic models are highly correlated with each variable separately (not shown) and their product (H). In other words, our results hold true even if we ignore SIT because the variations in SIT are reflected in those of SIC .

To first order, the results shown here provide a good representation of the significant role of air temperature in driving sea ice variations. In addition, we have shown that this variability is mostly related to remote forcing, but there is still a significant role at the local scale. This last point

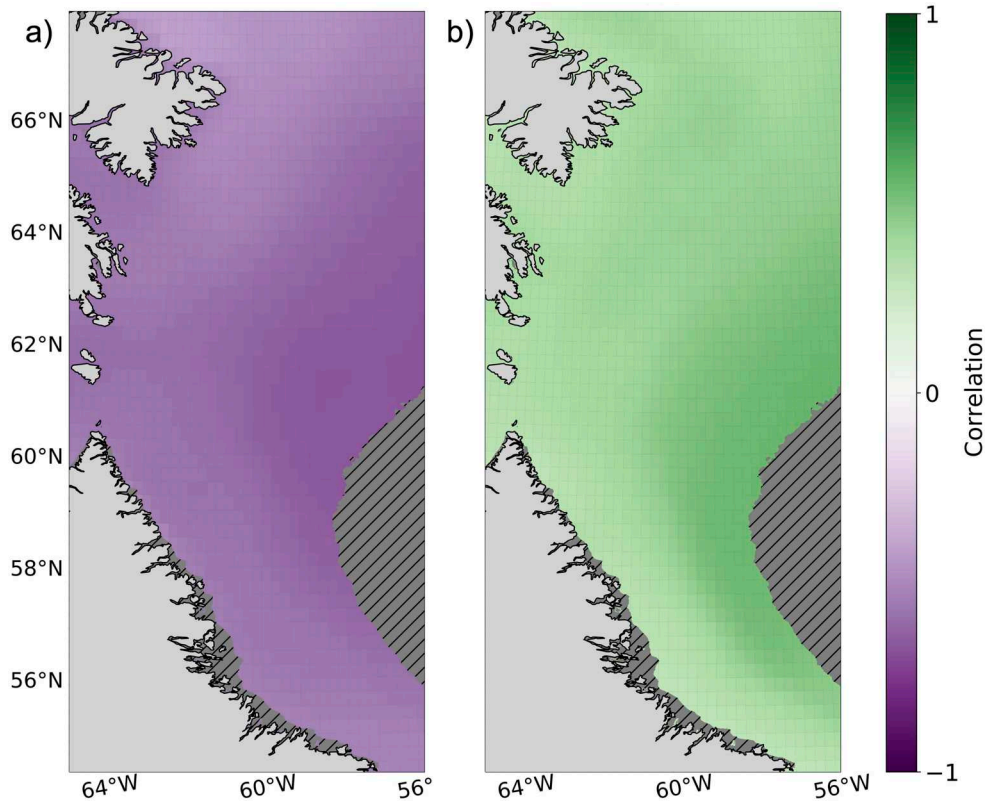


Fig. 7 Correlation maps for the principal components (PCs) and 2 m air temperature (SAT). Shown are lag -1 correlations between (a) Mode 1 and (b) Mode 2 with SAT. The PC time series lag SAT by one month (seasonally averaged SAT anomalies from November to March correlated with the ice data from December to April). The landfast ice zone and the offshore zone with climatologically rare ice presence are masked out with grey hatches.

is consistent with that of Symonds (1986) who reported that ice growth of 1 cm/day can be sustained at 55°N. Also, Yao et al. (2000) modelled up to 1 m of ice growth along the inner shelf, with net melt up to 2 m along the outer shelf. We also note that since air temperature anomalies are very large in spatial scale, it is difficult to quantify exactly how much of the variability is influenced by local versus remote forcing in this study. Also, since ice floes reach most of their maximum thickness before it arrives on the LS, local thermodynamic effects are likely more important in the melt stage, which we have ignored here due to limitations in the dataset (described in Section 2a).

b Comparisons to the Arctic

Our results illustrate a common, overarching connection between the Arctic Ocean and the Labrador Shelf: sea ice changes are driven by a warming atmosphere. We have shown that a large part of sea ice variability on the LS is driven by air temperature anomalies. The long-term trends of sea ice volume and thickness are also driven by local thermodynamics, which is consistent with observations in the Arctic (Cai, Beletsky et al., 2021; Cai, Wang et al., 2021). Rapid anthropogenic warming has led to a significant decline in Arctic sea ice extent and thickness and increased number of anomalous ice seasons for Arctic coastal

communities (Meier & Stroeve, 2022). Many of these communities have reported thinning landfast ice conditions (Laidler et al., 2009), and Cooley et al. (2020) found reductions in landfast duration across nearly all 28 Arctic communities in their study (their study did not include Nunat-siavut). We presume that the landfast ice is a distinctly unique system from the pack ice on the LS and therefore deserves a different treatment in a separate, future study.

We did a separate EOF analysis on H using SIT from the thickest category of the CISDA only (not shown), which presented very similar EOF patterns compared to average H for the first two modes. The first mode from this analysis is more strongly correlated with local air temperature anomalies everywhere in the domain and both of the thermodynamic ice growth models (FDD: 0.88; heat flux model: 0.87, $p < 0.05$). This result suggests that the thickest ice types in the region, which largely consist of MYI and old ice floes from the Arctic, are more thermodynamically driven than the thinner ice types, which are mostly locally formed.

7 Conclusion

There has been a dramatic loss of sea ice in the Arctic over the past four decades, but this does not appear to be the case on the Labrador Shelf. However, the growing unpredictability of year-to-year variations in sea ice conditions and associated

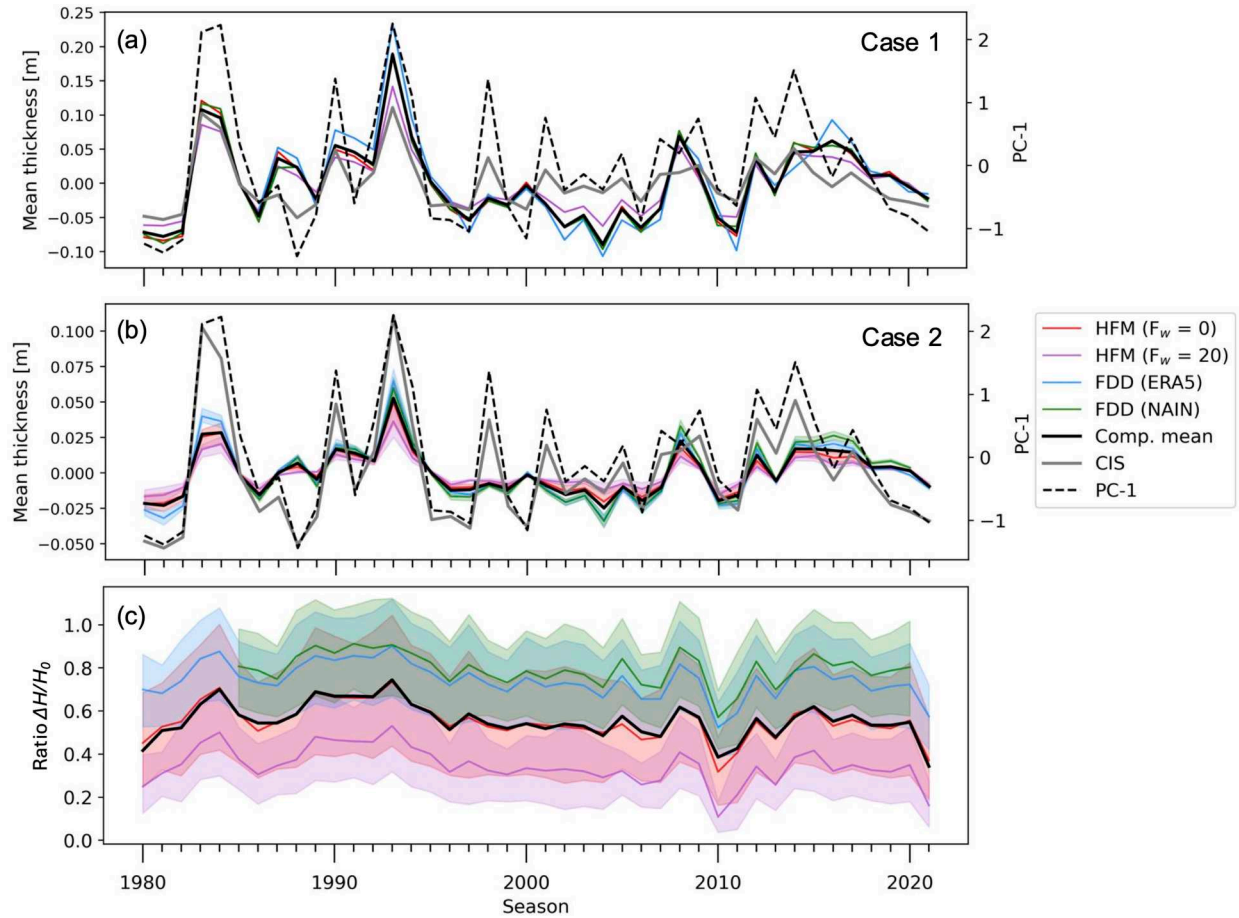


Fig. 8 Results from the ice growth models. Normalized PC-1 (dashed line) and modelled mean ice thickness (H) anomalies are plotted for (a) Case 1 and (b) Case 2. The ratios of ice growth on the LS (ΔSIT) to the initial thickness (H_0) for Case 2 are shown in (c). The colored lines represent different models: heat flux model (HFM) with $F_w = 0 \text{ Wm}^{-2}$ (red line), HFM with $F_w = 20 \text{ Wm}^{-2}$ (purple line), the freezing degree day (FDD) model forced with air temperature (SAT) from ERA5 (blue line) and NAIN (Green line). In (b) and (c), the shading represents the range across the three transit times (19, 39, and 97 days), and the solid colored lines are the mean. The black solid line is the composite mean across all models and the grey line is domain-averaged H from the CIS charts.

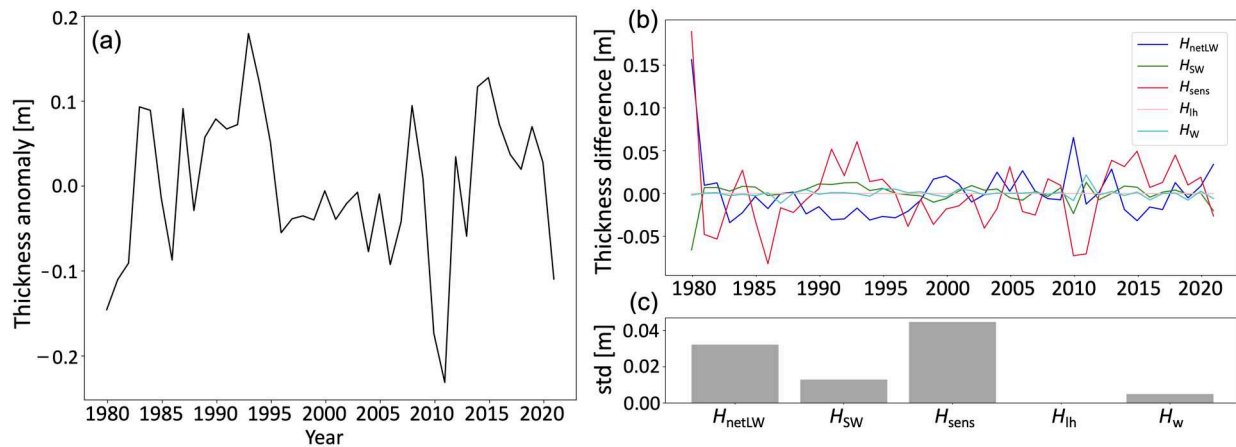


Fig. 9 Heat flux model for sea ice thickness including the role of each heat flux term. Each time series in (b) represents the difference in sea ice thickness (ΔSIT) between the model run with all forcing variables (solid line in (a)) and a model run with one flux term removed, indicated in the legend. Standard deviations of each time series in (b) is shown in (c).

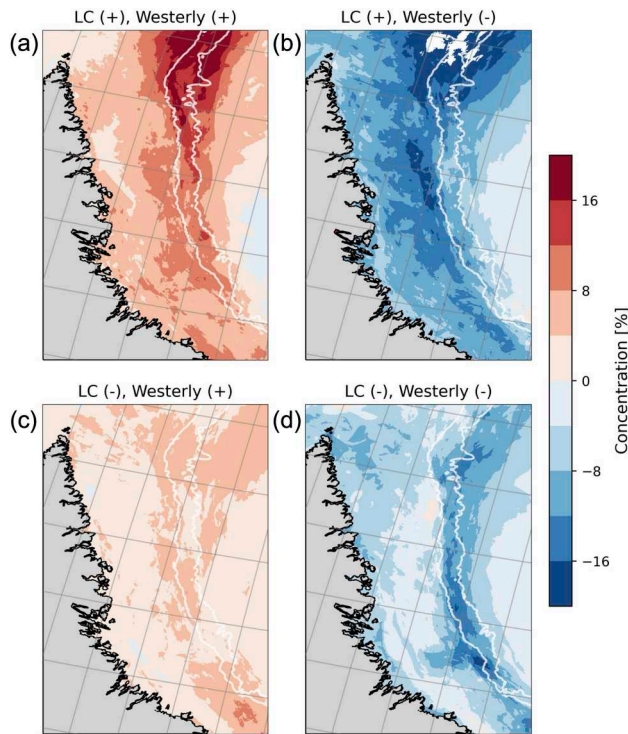


Fig. 10 Reconstructed sea ice concentration (*SIC*) anomaly maps. Each map represents the average *SIC* anomaly for time periods of (a) strong Labrador Current (LC) and strong westerlies, (b) strong LC and weak westerlies, (c) weak LC and strong westerlies and (d) weak LC and weak westerlies, with strong and weak defined as above and below the climatological mean.

extremes are raising concern for the regional ecosystems (Greene et al., 2012) and coastal communities who rely on the integrity of the ice each year. Based on 41 years of Canadian Ice Service sea ice charts, sea ice on the northern Labrador coast and shelf has a consistent but small downward trend. The most notable trends for ice thickness, mean ice thickness and concentration appear in and east of the Marginal Ice Zone during the peak phase, suggesting a reduction in ice cover eastward from the shelf edge. Our EOF analysis revealed that 67.8% of the total variability of mean ice thickness can be explained by the first two EOF modes. The leading mode (Mode 1) accounts for 52.6% of the variability and is the largest, single physically independent mode. Our

results suggest that over the growth and peak stages of the sea ice season, remote air temperature anomalies upstream of the Labrador Shelf are the primary drivers of sea ice variability and trends on the shelf. A smaller, but non-negligible fraction of the variability is associated with local (i.e. shelf-scale) air temperature anomalies. Additionally, a large fraction of mean ice thickness variability can be reconstructed using simple thermodynamic ice growth models. Mode 2 (12.9%) has a spatial dipole pattern separating on- and off- shelf regions, which may be linked to coupled effects between ocean currents and wind drift. Under a continuously warming climate, we anticipate more intense extreme ice seasons. Although the spatial scale in this study is too large to be directly meaningful for communities, adding this larger-scale perspective of the region is a necessary contribution to conducting future work at community-relevant scales, which is more pressing than ever as residents in the Arctic and sub-Arctic zones are the most vulnerable to future climate change.

Acknowledgments

The authors would like to thank Clark Richards and Dewey Dunnington for gridding the sea ice charts, Adrienne Tivy for her support and guidance in using the sea ice charts, and the anonymous reviewers for their detailed feedback and recommendations.

Disclosure statement

No potential conflict of interest was reported by the author(s).

Funding

Support for this work was received from National Sciences and Engineering Research Council of Canada Discovery Grant [RGPIN-2018-05255], Crown-Indigenous Relations and Northern Affairs Canada through an award from the Climate Change and Preparedness in the North program, the Ocean Frontier Institute through an award from the Canada First Research Excellence Fund, and ArcticNet, a Network of Centres of Excellence Canada.

References

Barber, D. G., Babb, D. G., Ehn, J. K., Chan, W., Matthes, L., Dalman, L. A., Campbell, Y., Harasyn, M. L., Firoozy, N., Theriault, N., Lukovich, J. V., Zagon, T., Papakyriakou, T., Capelle, D. W., Forest, A., & Garipey, A. (2018). Increasing mobility of high arctic sea ice increases marine hazards off the east coast of Newfoundland. *Geophysical Research Letters*, 45(5), 2370–2379. <https://doi.org/10.1002/grl.v45.5>

Brice-Bennett, C., & Labrador Inuit Association (1977). *Our footprints are everywhere: Inuit land use and occupancy in Labrador*. [Nain, Nfld.] Labrador Inuit Association.

Cai, Q., Beletsky, D., Wang, J., & Lei, R. (2021). Interannual and decadal variability of arctic summer sea ice associated with atmospheric teleconnection patterns during 1850–2017. *Journal of Climate*, 34(12), 9931–9955. <https://doi.org/10.1175/JCLI-D-20-0791.1>

Cai, Q., Wang, J., Beletsky, D., Overland, J., Ikeda, M., & Wan, L. (2021). Accelerated decline of summer Arctic sea ice during 1850–2017 and the amplified Arctic warming during the recent decades. *Environmental Research Letters*, 16(3), 034015. <https://doi.org/10.1088/1748-9326/abdb5f>

Canadian Coast Guard (2022). *Ice navigation in Canadian waters* (6th ed.). Fisheries and Oceans Canada.

Canadian Ice Service (2005). *CIS: MANICE (manual of ice)*. <https://www.canada.ca/en/environment-climate-change/services/weather-manuals-documentation/manice-manual-of-ice/chapter-3.html>

- Canadian Ice Service (2007). *CISDA – Regional charts: Canadian ice service ice regime regions (CISIRR) and sub-regions with associated data quality indices*. https://ice-glaces.ec.gc.ca/IA/_DOC/cisads_no_003_e.pdf
- Cavalieri, D. J., & Parkinson, C. L. (2012). Arctic sea ice variability and trends, 1979–2010. *The Cryosphere*, 6(4), 881–889. <https://doi.org/10.5194/tc-6-881-2012>
- Close, S., Herbaut, C., Houssais, M., & Blaziot, A. (2018). Mechanisms of interannual- to decadal-scale winter labrador sea ice variability. *Climate Dynamics*, 51(7-8), 2485–2508. <https://doi.org/10.1007/s00382-017-4024-z>
- Cooley, S. W., Ryan, J. C., Smith, L. C., Horvat, C., Pearson, B., Dale, B., & Lynch, A. H. (2020). Coldest Canadian Arctic communities face greatest reductions in shorefast sea ice. *Nature Climate Change*, 10(6), 533–538. <https://doi.org/10.1038/s41558-020-0757-5>
- Cuny, J., Rhines, P. B., & Kwok, R. (2005). Davis strait volume, freshwater and heat fluxes. *Deep Sea Research Part I: Oceanographic Research Papers*, 52(3), 519–542. <https://doi.org/10.1016/j.dsr.2004.10.006>
- Cyr, F., Coyne, J., Snook, S., Bishop, C., Galbraith, P. S., Chen, N., & Han, G. (2024a). Physical oceanographic conditions on the newfoundland and labrador shelf during 2023. *Canadian Technical Report of Hydrography and Ocean Sciences*, 377, 4–53.
- Cyr, F., Coyne, J., Snook, S., Bishop, C., Galbraith, P. S., Chen, N., & Han, G. (2024b). Physical oceanographic conditions on the newfoundland and labrador shelf during 2023. *Canadian Technical Report of Hydrography and Ocean Sciences*, 382, 4–54.
- Cyr, F., Snook, S., Bishop, C., Galbraith, P., Chen, N., & Han, G. (2022). Physical oceanographic conditions on the newfoundland and labrador shelf during 2021. *DFO Canadian Science Advisory Secretariat Doc*, 2022/040, 4–48.
- Davis, R. E. (1976). Predictability of sea surface temperature and sea level pressure anomalies over the North Pacific Ocean. *Journal of Physical Oceanography*, 6(3), 249–266. [https://doi.org/10.1175/1520-0485\(1976\)006<0249:POSSTA;2.0.CO;2](https://doi.org/10.1175/1520-0485(1976)006<0249:POSSTA;2.0.CO;2)
- Deser, C., Holland, M., Reverdin, G., & Timlin, M. (2002). Decadal variations in labrador sea ice cover and North Atlantic sea surface temperatures. *Journal of Geophysical Research*, 107(C5), 1–12. <https://doi.org/10.1029/2000JC000683>
- Dunbar, M. (1973). Ice regime and ice transport in nares strait. *Arctic*, 26(4), 282–291. <https://doi.org/10.14430/arctic2927>
- Environment and Climate Change Canada (ECCC) (2018). *Adjusted and homogenized canadian climate data (AHCCD)*. <https://open.canada.ca/data/en/dataset/9c4ebc00-3ea4-4fe0-8bf2-66cfe1cddd1d>
- Florindo-López, C., Bacon, S., Aksenov, Y., Chafik, L., Colbourne, E., & Holliday, N. P. (2020). Arctic ocean and Hudson Bay freshwater exports: New estimates from seven decades of hydrographic surveys on the labrador shelf. *Journal of Climate*, 33(20), 8849–8868. <https://doi.org/10.1175/JCLI-D-19-0083.1>
- Galbraith, P. S., Chassé, J., Dumas, J., Shaw, J. L., Caverhill, C., Lefavre, D., & Laffleur, C. (2022). Physical oceanographic conditions in the Gulf of St. Lawrence during 2021. *DFO Canadian Science Advisory Secretariat Doc*, 2022/034, 4–83.
- Galbraith, P. S., Sévigny, C., Bourgault, D., & Dumont, D. (2024). Sea ice interannual variability and sensitivity to fall oceanic conditions and winter air temperature in the Gulf of St. Lawrence, Canada. *Journal of Geophysical Research: Oceans*, 129(7), e2023JC020784. <https://doi.org/10.1029/2023JC020784>
- Goosse, H., Campin, J. M., Deleersnijder, E., Mathieu, P. P., M. Á. Morales Maqueda, & Tartinville, B. (2000). Description of the CLIO model.
- Greene, C. H., Monger, B. C., McGarry, L. P., Connelly, M. D., Schnepf, N. R., Pershing, A. J., Pershing, A. J., Belkin, I. M., Fratantoni, P. S., Mountain, D. G., Pickart, R. S., Ji, R., Bisagni, J. J., Chen, C., Hakkinen, S. M. A., Haijvogel, D. B., Wang, J., Head, E., Smith, P., & Conversi, A. (2012). Recent arctic climate change and its remote forcing of northwest atlantic shelf ecosystems. *Oceanography*, 25(2), 208–213. <https://doi.org/10.5670/oceanog>
- Haas, C., Hendricks, S., Eicken, H., & Herber, A. (2010). Synoptic airborne thickness surveys reveal state of Arctic sea ice cover. *Geophysical Research Letters*, 37(9), L09501. <https://doi.org/10.1029/2010GL042652>
- Han, G., Lu, Z., Wang, Z., Helbig, J., Chen, N., & Deyoung, B. (2008). Seasonal variability of the labrador current and shelf circulation off newfoundland. *Journal of Geophysical Research*, 113(C10), C10013. <https://doi.org/10.1029/2007JC004376>
- Hersbach, H., Bell, B., Berrisford, P., Biavati, G., Horányi, A., & J. Muñoz Sabater (2023). *ERA5 hourly data on single levels from 1940 to present*. Copernicus Climate Change Service (C3S) Climate Data Store (CDS).
- Howell, S. E. L., Babb, D. G., Landy, J. C., Moore, G. W. K., Montpetit, B., & Brady, M. (2024). *Monthly sea ice area and volume flux values for Davis Strait, Nares Strait, Lancaster Sound, and Jones Sound from October 2016 to September 2022 [Dataset]*. <https://crd-data-donnees-rc.gc.ca/CPS/products/IceFlux/Publications/BaffinBay-Fluxes-GRL-2024.xlsx>
- Hurrell (2003). *Nao index data [Dataset]*. Updated regularly. <https://climatedataguide.ucar.edu/climate-data/hurrell-north-atlantic-oscillation-nao-index-station-based>
- Kvamstø, N. G., Skeie, P., & Stephenson, D. B. (2004). Impact of labrador sea-ice extent on the North Atlantic oscillation. *International Journal of Climatology*, 24(5), 603–612. <https://doi.org/10.1002/joc.v24:5>
- Laidler, G. J., Ford, J. D., Gough, W. A., Ikummaq, T., Gagnon, A. S., Kowal, S., Qrunnut, K., & Irgaut, C. (2009). Travelling and hunting in a changing Arctic: Assessing inuit vulnerability to sea ice change in igloolik, nunavut. *Climatic Change*, 94(3), 363–397. <https://doi.org/10.1007/s10584-008-9512-z>
- Lazier, J. R. N., & Wright, D. G. (1993). Annual velocity variations in the labrador current. *Journal of Physical Oceanography*, 23(4), 659–678. [https://doi.org/10.1175/1520-0485\(1993\)023<0659:AVVITL;2.0.CO;2](https://doi.org/10.1175/1520-0485(1993)023<0659:AVVITL;2.0.CO;2)
- Lebedev, V. (1938). Rost l'da v arkticheskikh rekakh i moriakh v zavisimosti ot otritsatel'nykh temperatur vozdukh. *Problemy Arktiki*, 5(6), 9–25.
- Jean-Michel, L., Eric, G., Romain, B., Gilles, G., Angélique, M., Marie, D., Clément, B., Mathieu, H., Olivier, L. G., Charly, R., Tony, C., Charles-Emmanuel, T., Florent, G., Giovanni, R., Mounir, B., Yann, D., & Pierre-Yves, L. T. (2021). The copernicus global 1/12° oceanic and sea ice GLORYS12 reanalysis the copernicus global 1/12° oceanic and sea ice GLORYS12 reanalysis. *Frontiers in Earth Science*, 9, 698876. <https://doi.org/10.3389/feart.2021.698876>
- Loder, J., Petrie, B., & Gawarkiewicz, G. (1998). The coastal ocean off north-eastern North America: A large-scale view. In *The Sea, Volume 11: The global coastal ocean – regional studies and syntheses* (Vol. 11, pp. 105–133). Wiley & Sons.
- Massonnet, F., Vancoppenolle, M., Goosse, H., Docquier, D., Fichet, T., & Blanchard-Wrigglesworth, E. (2018). Arctic sea-ice change tied to its mean state through thermodynamic processes. *Nature Climate Change*, 8(7), 599–603. <https://doi.org/10.1038/s41558-018-0204-z>
- Maykut, G. (1986). The surface heat and mass balance. In N. Untersteiner (Ed.), *The geophysics of sea ice*. Springer US.
- Maykut, G., & Untersteiner, N. (1969). *Numerical prediction of the thermodynamic response of arctic sea ice to environmental changes*. The Rand Corporation. RM-6093-PR.
- Meier, W. N., & Stroeve, J. (2022). An updated assessment of the changing arctic sea ice cover. *Oceanography*, 35(3/4), 10–19.
- Mitchell, J., Dzerdzevskii, B., Flohn, H., Hofmeyer, W., Lamb, H., Rao, K., & Wallen, C. (1966). *Climatic change*. World Meteorological Organization TP 100 79.
- Overland, J. E., & Preisendorfer, R. W. (1982). A significance test for principal components applied to a cyclone climatology. *Monthly Weather Review*, 110(1), 1–4. [https://doi.org/10.1175/1520-0493\(1982\)110<0001:ASTFPC;2.0.CO;2](https://doi.org/10.1175/1520-0493(1982)110<0001:ASTFPC;2.0.CO;2)
- Parkinson, C. L., & Comiso, J. C. (2013). On the 2012 record low Arctic sea ice cover: Combined impact of preconditioning and an August storm. *Geophysical Research Letters*, 40(7), 1356–1361. <https://doi.org/10.1002/grl.v40.7>
- Peterson, I., Pettipas, R., & Rosing-Asvid, A. (2015). Trends and variability in sea ice and icebergs off the Canadian east coast. *Atmosphere-Ocean*, 53(5), 582–594. <https://doi.org/10.1080/07055900.2015.1057684>
- Peterson, I., & Symonds, G. (1988). Ice floe trajectories off Labrador and eastern Newfoundland: 1985–1987. pp. 5–101.

Prinsenberg, S. J., Peterson, I. K., Narayanan, S., & Umoh, J. U. (1997). Interaction between atmosphere, ice cover, and ocean off Labrador and Newfoundland from 1962 to 1992. *Canadian Journal of Fisheries and Aquatic Sciences*, 54(S1), 30–39. <https://doi.org/10.1139/f96-150>

Semtner, A. J. (1976). A model for the thermodynamic growth of sea ice in numerical investigations of climate. *Journal of Physical Oceanography*, 6(3), 379–389. [https://doi.org/10.1175/1520-0485\(1976\)006<0379:AMFTTG>2.0.CO;2](https://doi.org/10.1175/1520-0485(1976)006<0379:AMFTTG>2.0.CO;2)

Serreze, M. C., & Francis, J. A. (2006). The arctic amplification debate. *Climatic Change*, 76(3), 241–264. <https://doi.org/10.1007/s10584-005-9017-y>

Straneo, F., & Saucier, F. (2008). The outflow from Hudson strait and its contribution to the Labrador current. *Deep Sea Research Part I: Oceanographic Research Papers*, 55(8), 926–946. <https://doi.org/10.1016/j.dsr.2008.03.012>

Symonds, G. (1986). Seasonal ice extent on the northeast Newfoundland shelf. *Journal of Geophysical Research: Oceans*, 91(C9), 10718–10724. <https://doi.org/10.1029/JC091iC09p10718>

Tang, C. C. L., Ross, C. K., Yao, T., Petrie, B., DeTracey, B. M., & Dunlap, E. (2004). The circulation, water masses and sea-ice of Baffin Bay. *Progress in Oceanography*, 63(4), 183–228. <https://doi.org/10.1016/j.pocean.2004.09.005>

Turnbull, I. D., & Taylor, R. S. (2018). Coastal Labrador land-fast ice: Relative influences of the thermodynamic forcings on the break-up and effects of clouds, humidity, and wind. *Journal of Ocean Technology*, 13(1), 77–105.

Wagner, T. J. W., & Eisenman, I. (2015). How climate model complexity influences sea ice stability. *Journal of Climate*, 28(10), 3998–4014. <https://doi.org/10.1175/JCLI-D-14-00654.1>

Wettlaufer, J. S. (1991). Heat flux at the ice-ocean interface. *Journal of Geophysical Research: Oceans*, 96(C4), 7215–7236. <https://doi.org/10.1029/90JC00081>

Yao, T., Tang, C. L., & Peterson, I. K. (2000). Modeling the seasonal variation of sea ice in the Labrador sea with a coupled multicategory ice model and the Princeton ocean model. *Journal of Geophysical Research: Oceans*, 105(C1), 1153–1165. <https://doi.org/10.1029/1999JC900264>

Appendix A Heat Flux Model

The heat flux model presented in this paper is largely based on the one-dimensional model presented in Semtner (1976, hereafter referred to as SEM), which in turn is based on the model presented in Maykut and Untersteiner (1969). The model accounts for heat fluxes at the ice-atmosphere interface and heat fluxes from the surface ocean through the ice slab. The sea ice vertical temperature profile and thickness of the ice slab are governed by the one-dimensional heat equation as per SEM:

$$(\rho c)_i \frac{\partial T_i}{\partial t} = k_i \frac{\partial^2 T_i}{\partial z^2} = \frac{\partial F_c}{\partial z} \quad (A1)$$

where $(\rho c)_i$ is the volumetric heat capacity of ice, T_i is the ice temperature (K), t is time (seconds), k_i is the thermal conductivity of ice, F_c is the conductive flux within the ice (Wm^{-2}), and z is the depth in the ice slab (m; positive upwards) with $z = 0$ defined at the ice surface. For reasonably thin ice, the temperature profile inside the slab is assumed to be linear (Maykut, 1986). Therefore,

$$F_c = -k_i \frac{\partial T}{\partial z} = -k_i \frac{T_s - T_b}{SIT} \quad (A2)$$

where T_s and T_b are the temperatures at the ice surface and bottom, respectively, and SIT is the ice thickness. T_b is fixed

at the freezing point of seawater (-1.8°C), and T_s is free to evolve and must be solved using a surface heat flux balance. At the surface, the heat balance is

$$(1 - \alpha)F_{\text{inSW}} + F_{\text{netLW}} + F_{\text{sens}} + F_{\text{lh}} + F_c = 0 \quad (A3)$$

where α is the ice surface temperature-dependent albedo (0.8 for bare ice, 0.5 for melting ice; Goosse et al., 2000), and the heat fluxes (F , Wm^{-2}) are: F_{inSW} the downward shortwave radiation at the ice surface, F_{netLW} the net longwave radiation at the ice surface, F_{sens} the sensible heat flux at the ice surface, and F_{lh} the net latent heat flux due to sublimation at the ice surface. External fluxes are positive towards the ice and heat fluxes inside the ice (F_c) are positive upward. The net longwave radiation can be expressed as incoming (F_{LW}) minus outgoing longwave radiation: $F_{\text{netLW}} = F_{\text{LW}} - \sigma T_s^4$ with σ the Stefan-Boltzmann constant. The outgoing longwave radiation is parametrised as a simple blackbody. The sensible heat flux is parametrised as a function of the wind speed, U_{wd} , $F_{\text{sens}} = \rho_a c_{p,a} c_{\text{sh}} U_{\text{wd}} (T_a - T_s)$ where ρ_a is the air density, $c_{p,a}$ the air specific heat capacity and c_{sh} the transfer coefficient. Equation (A3) can then be written as

$$\begin{aligned} (1 - \alpha)F_{\text{inSW}} + F_{\text{LW}} - \sigma T_s^4 + \rho_a c_{p,a} c_{\text{sh}} U_{\text{wd}} (T_a - T_s) \\ + F_{\text{lh}} \\ = k_i \frac{T_s - T_b}{SIT} \end{aligned} \quad (A4)$$

which can be rearranged as a 4th order polynomial of the surface temperature T_s . A polynomial study shows that there are only two real roots, of which only one of them can be positive (when using Kelvin units) and thus physical.

At the ice bottom, the heat balance is between the oceanic heat flux and conductive heat flux:

$$\left. \frac{\partial SIT}{\partial t} \right|_{\text{bot}} = \frac{1}{L_i} (F_c - F_w) = -\frac{1}{L_i} \left(k_i \frac{T_s - T_b}{SIT} - F_w \right) \quad (A5)$$

where L_i is the sea ice latent heat capacity (Jm^{-3}), $\left. \frac{\partial SIT}{\partial t} \right|_{\text{bot}}$ the ice growth rate at the bottom, and F_w the oceanic heat flux. The boundary conditions for Eqs. (A1) and (A2) ensure that any imbalance at the surface or bottom causes the ice thickness to change. At the surface, melting occurs if T_s is greater than or equal to the melting point of sea ice ($T_m = 0^\circ\text{C}$). So we must add a melting term, $-L_i \left. \frac{\partial SIT}{\partial t} \right|_{\text{top}}$, to the right side of Eq. (A4). If $T_s < T_m$, then $\left. \frac{\partial SIT}{\partial t} \right|_{\text{top}} = 0$ as we cannot have ice growth at the surface. At the bottom, any imbalance in Eq. (A5) will lead to growth or melt. Also, since F_c is constant, then the conductive flux term at the ice-ocean boundary is the same as the conductive heat flux at the ice-air boundary. The total ice growth-melt rate is the sum of the surface melt and the bottom growth-melt, as described by the following equation

$$\frac{\partial SIT}{\partial t} = \left. \frac{\partial SIT}{\partial t} \right|_{\text{top}} + \left. \frac{\partial SIT}{\partial t} \right|_{\text{bot}} \quad (A6)$$

From this equation, we obtain the following conditional expression which we use to solve for the ice growth at each

time step:

$$\frac{\partial SIT}{\partial t} = \begin{cases} -\frac{1}{L_i} (k_i \frac{T_s - T_b}{SIT} + F_w) & T_s < T_m \\ -\frac{1}{L_i} ((1 - \alpha)F_{SW} + F_{LW} - \sigma T_s^4 + \rho_a c_{p,a} c_{sh} U_{wd} (T_a - T_s) + F_{lh} + F_w) & T_s = T_m \end{cases} \quad (A7)$$

We solve the model using the standard Euler-backward scheme in the programming language of Python. We use an hourly time step Δt from 1979 September 1 00:00:00 UTC to 2021

May 1 00:00:00 UTC 2021 with an initial thickness ($SIT|_{t=0}$) of 0.01 m and ice surface temperature ($T_s|_{t=0}$) of -10°C . Our input forcings are hourly variables from ERA5 (F_{LW} , F_{SW} , F_{lh} , U_{wd}). We also implement the following conditions to ensure the numerical solution is always physical. Ice thickness can never be negative, so if $SIT(t) = 0$ and $\frac{\partial SIT}{\partial t}(t) < 0$, then we set $\frac{\partial SIT}{\partial t}(t) = 0$. Every year, SIT is reset to the initial condition for all days in August. This ensures that the modelled ice season represents the LS ice season which does not have ice year-round (otherwise, if the ice never fully melted during the summer, the initial thickness for the following season would be too thick).